ADVANCED ENERGY MATERIALS
www.advenergymat.de

Polymer-Assisted Morphology Regulation Enables 18.3%–Efficiency in *o*-Xylene Processed All-Small-Molecule Organic Solar Cells

Jia Wang, Wenying Zhou, Wenkai Zhao, Baofa Lan, Jiaying Wang, Wanying Feng, Miaomiao Li, Adiljan Wupur, Weifei Fu, Guankui Long, Bin Kan,* and Yongsheng Chen*

All-small-molecule organic solar cells (ASM-OSCs) offer advantages in structure definition and synthesis but suffer from morphology control challenges due to donor-acceptor miscibility. Herein, a simple yet highly effective morphology regulation strategy is introduced by incorporating a small amount of polymer donor PM6 into the BTR-Cl: Y6 binary system. The chain structure of PM6 further directs epitaxial growth of the BTR-Cl phase, driving the formation of a continuous fibrillar network within the donor domains. Consequently, additive-free and o-xylene processed devices exhibit superior charge dynamics, significantly boosting short-circuit current density and fill factor, achieving a champion efficiency of 18.3%—among the highest for non-halogenated solvent processed small donor-small acceptor dominated OSCs. Besides, introducing PM1 into the BTR-Cl: Y6 system also achieved 18.0% PCE. Moreover, the devices also show exceptional thickness insensitivity—retaining 96% of peak efficiency even at 300 nm active-layer thickness. Leveraging the advantage with non-halogenated solvents, large-area OSCs (13.5 cm^2) achieving 12.2% PCE are successfully fabricated. Flexible devices delivered 14.9% efficiency and maintained 92% initial PCE after 800 bending cycles, primarily attributed to PM6's long-chain structure, enhancing the crack-onset strain of the active layer. This work provides a facile morphology-regulation strategy for high-performance small donor-small acceptor dominated OSCs.

1. Introduction

In recent years, advancements in device engineering, coupled with innovations in polymer donors and non-fullerene small-molecule acceptors, have propelled the power conversion efficiency (PCE) of organic solar cells (OSCs)OSCs to 21%.[1–5] Among the diverse organic photovoltaic material systems, all-small-molecule active layers have gained significant attention due to their well-defined structures and high batch-to-batch reproducibility.[6–8] Through explorations of strategies such as molecular material design, interface optimization, and device engineering, the PCEs of all-small-molecule organic solar cells (ASM-OSCs) have exceeded 18%.[9,10] Note that the advancement of high-performance OSCs processed from environmentally benign non-halogenated solvents is particularly critical for scalable manufacturing and commercial viability.[11] For example, through synergistic application of hot spin-coating and solvent vapor annealing strategies, Li et al. optimized the morphology of H31:Y6 blend film and attained a PCE of 14.4% for the toluene-processed ASM-OSCs.[12] In another study, Li et al. developed a new small-molecular donor BM-ClEH and demonstrated a 16.1% efficient THF-processed OSC.[13] However, achieving optimal active layer morphology in these systems, particularly those based on small-molecular donors and acceptors, remains a significant challenge. Consequently, the efficiency of devices processed with non-halogenated solvents still lags behind that of devices using halogenated solvents.[14,15]

This disparity primarily stems from significant differences in molecular size, polarity, and volatility between non-halogenated

J. Wang, W. Zhou, W. Zhao, B. Lan, J. Wang, G. Long, B. Kan
School of Materials Science and Engineering
National Institute for Advanced Materials
Nankai University
Tianjin 300350, China
E-mail: kanbin04@nankai.edu.cn

The ORCID identification number(s) for the author(s) of this article can be found under https://doi.org/10.1002/aenm.202504576

DOI: 10.1002/aenm.202504576

J. Wang, W. Feng, Y. Chen
State Key Laboratory and Institute of Elemento-Organic Chemistry
Frontiers Science Center for New Organic Matter
The Centre of Nanoscale Science and Technology and Key Laboratory of Functional Polymer Materials
Renewable Energy Conversion and Storage Center (RECAST)
College of Chemistry
Nankai University
Tianjin 300071, China
E-mail: 9820240058@nankai.edu.cn

and halogenated solvents.[16] The high boiling point and slow evaporation kinetics of non-halogenated solvents readily induce excessive molecular aggregation, inhomogeneous phase separation, and disordered molecular orientation within the active layer.[17] These morphological defects ultimately impede exciton dissociation, charge transport, and collection efficiency. Consequently, critical device performance parameters, particularly the fill factor (*FF*) and short-circuit current density (J_{SC}), suffer from constraints. And a significant efficiency decrease is also observed under thick-film conditions (>300 nm).[9] Beyond these, enhancing the mechanical robustness of the active layer is equally crucial for advancing the development of small molecule-dominated OSCs. The inherent strong crystallinity of small molecules tends to generate oversized phase-separated domains,[18] while their rigid molecular backbones and high crystallinity result in a crack-onset strain (COS) substantially inferior to that of polymer-based systems, posing challenges for flexible device development. Therefore, designing effective strategies to precisely control the morphology of small molecule-dominated OSCs processed from non-halogenated solvents, while simultaneously improving the mechanical properties of the active layer, is urgently needed. Such advancements are vital for promoting the development of high-performance, stable, and large-area-fabricable small molecule-dominated OSCs.[13,14]

In this work, we proposed a simple yet highly effective morphology regulation strategy by introducing a small amount of polymer donor PM6 as a morphology regulator into the host BTR-Cl: Y6 binary system (**Figure 1a**). Temperature-dependent ultraviolet-visible (UV–vis) absorption and in situ UV–vis absorption measurements revealed that PM6 facilitates the formation of favorable pre-aggregation states of BTR-Cl and Y6 components in *o*-xylene (*o*-XY) solution. Furthermore, it accelerates film formation during spin-coating, mitigating excessive molecular aggregation typically caused by slow drying kinetics associated with non-halogenated solvents.[19] Crucially, PM6 incorporation promotes preferential face-on molecular packing and yields more uniform phase separation, in contrast to the excessive donor aggregation and disordered orientations observed in the binary film. Leveraging these combined advantages, the additive-free BTR-Cl: PM6:Y6 device demonstrated superior carrier dynamics, leading to significant enhancement in both J_{SC} and *FF*. Consequently, a champion PCE of 18.3% was achieved, representing one of the highest values reported for small-molecular materials dominated OSCs fabricated with non-halogenated solvents (Table S1, Supporting Information). To further validate this strategy, introducing PM1 into the BTR-Cl: Y6 system also achieved a high PCE of 18.0%. The BTR-Cl: PM6:Y6 system also exhibited excellent thickness insensitivity, achieving a notable PCE of 17.6% even when the active layer thickness was increased to 300 nm. The processing characteristics of the non-halogenated, high-boiling-point solvent *o*-XY also lay the foundation for large-area module development, as evidenced by a 13.5 cm^2 mini-module based on the BTR-Cl: PM6:Y6 blends that yields a PCE of 12.2%. In terms of flexible applications, the device fabricated on PEN substrate achieved a PCE of 14.9%, with PM6's long-chain structure significantly improving the active layer's COS and enabling the device to retain 92% of its initial efficiency after 800 bending cycles. This work provides a convenient and effective morphology control strategy to construct high-efficiency, stable, and thickness-insensitive small molecule-dominated OSCs.

2. Results and Discussion

The UV–vis absorption spectra of these materials in dilute *o*-XY solutions and thin films are plotted in Figure 1b and Figure S1 (Supporting Information). BTR-Cl, Y6, and PM6 exhibit complementary absorption, ranging from the visible light to the near-infrared region, ensuring excellent light-harvesting capability in relevant ternary blends. Notably, significant red-shifts in the maximum absorption peaks were observed for small molecules BTR-Cl and Y6 upon transitioning from dilute *o*-XY solutions to the thin-film state, measuring 75 and 137 nm, respectively, whereas PM6 exhibited only a minimal shift of 5 nm. Excessive red-shifts and pronounced aggregation of BTR-Cl and Y6 may indicate the formation of overly large, pure donor or acceptor phase domains.[20–22] Such domains are detrimental to the formation of a nanoscale interpenetrating network structure, consequently impairing the efficiency of exciton diffusion to the donor-acceptor interface and subsequent dissociation.[23,24]

Given that the distinct properties of PM6 may influence aggregation behavior within the active layer solution, we conducted temperature-dependent UV–vis absorption spectra on binary and ternary dilute solutions during controlled cooling (Figure 1c,d). The results show progressive red-shifts in the donor absorption region as the solution temperature decreased, with shifts of 21 nm for the binary blend and 30 nm for the ternary blend. This implies that the incorporation of PM6 may promote increased *J*-aggregation during cooling and facilitate the formation of pre-aggregates in solution.[17,25,26] In contrast, during film formation and solidification, PM6 predominantly functions as a morphological regulator. As shown in Figure 1e, the ternary blend film absorption exhibits a slight blue-shift compared to the binary blend, indicating that PM6 suppresses excessive aggregation of BTR-Cl and weakens the strong intermolecular interactions between BTR-Cl and Y6.[27]

To further investigate molecular packing and film crystallinity, we conducted grazing-incidence wide-angle X-ray scattering (GIWAXS).[28] The 2D GIWAXS patterns (Figure 1f,g) show that the binary blends exhibit distinct diffraction peaks along both in-plane (IP) and out-of-plane (OOP) directions, suggesting relatively disordered molecular orientations of BTR-Cl and

M. Li
School of Materials Science and Engineering
Tianjin Key Laboratory of Molecular Optoelectronic Science and Key Laboratory of Organic Integrated Circuits
Ministry of Education
and Collaborative Innovation Center of Chemical Science and Engineering (Tianjin)
Tianjin University
Tianjin 300072, China
A. Wupur
State Key Laboratory of Silicon and Advanced Semiconductor Materials
Department of Polymer Science and Engineering
Zhejiang University
Hangzhou 310027, China
W. Fu
Zhejiang University-Hangzhou Global Scientific and Technological Innovation Center
Hangzhou 311200, China

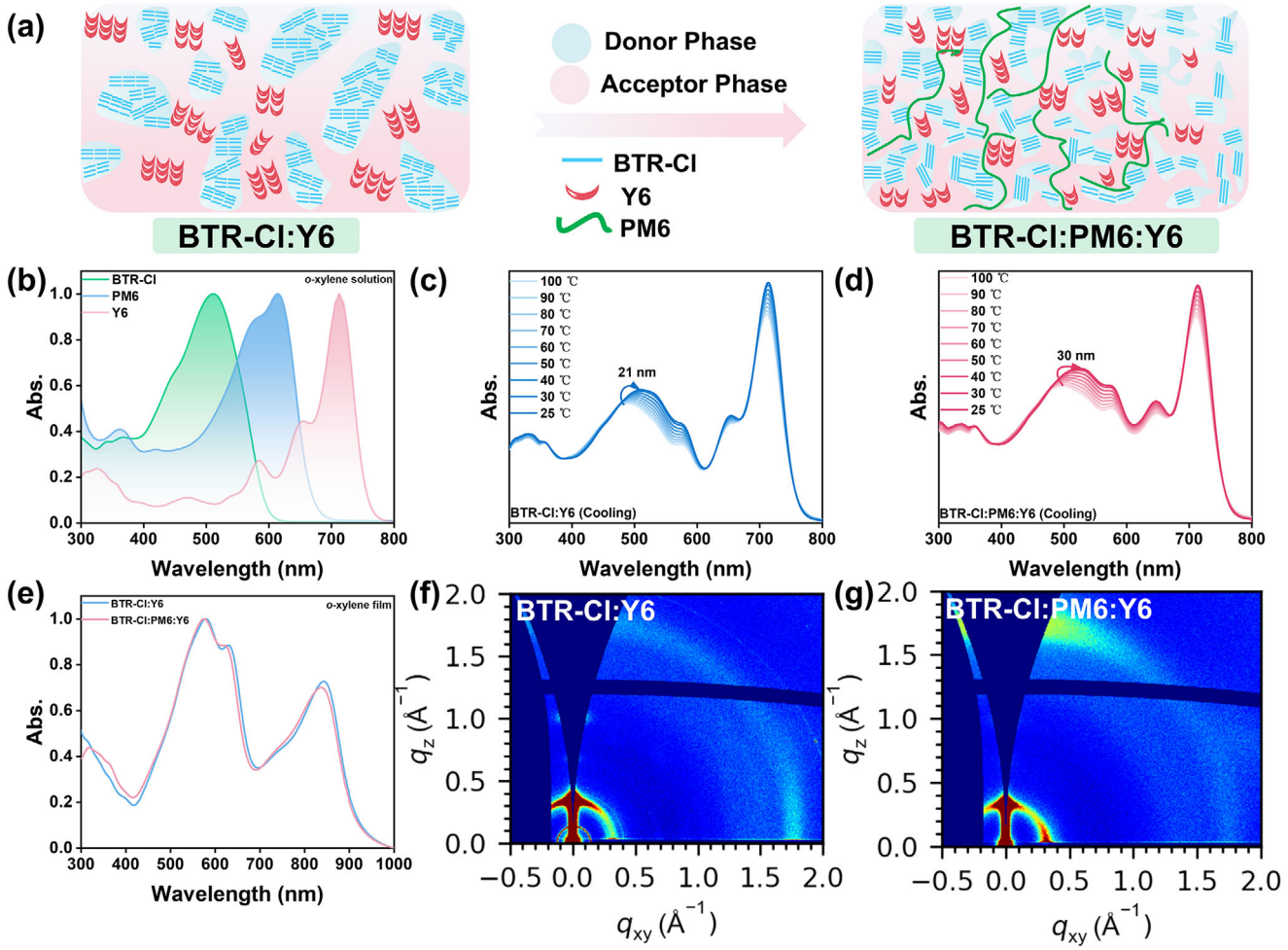

Figure 1. a) Schematic of the morphology and structure of the BTR-Cl: Y6 and BTR-Cl: PM6:Y6 films. b) Normalized UV–vis absorption spectra of BTR-Cl, PM6, and Y6 in *o*-XY solutions. Temperature-dependent UV–vis absorption spectra of c) BTR-Cl: Y6 and d) BTR-Cl: PM6:Y6 in *o*-XY solution at 100 °C to 25 °C, respectively. e) Normalized UV–vis absorption spectra of BTR-Cl: Y6 and BTR-Cl: PM6:Y6 blended films. (f, g) The 2D GIWAXS patterns of BTR-Cl: Y6 and BTR-Cl: PM6:Y6, respectively.

Y6. In contrast, the ternary blend displays a predominantly face-on molecular orientation. This orientation is likely facilitated by PM6's polymeric backbone, which suppresses disordered aggregation of BTR-Cl and promotes π–π stacking among the small molecules.[29] Analysis of the OOP (010) diffraction peak (Figure S2 and Table S2, Supporting Information) reveals that incorporating PM6 reduces the coherence length (CL) from 29.7 to 22.6 Å. This suggests that the BTR-Cl: PM6:Y6 system maintains ordered molecular packing while minimizing film defects.[30,31]

OSCs with a conventional architecture of indium tin oxide (ITO)/ 3,8-difluoroindolo[2,3-a]carbazole-11,12-diyl)bis(propane-3,1-diyl))bis(phosphonic acid) (3-BPIC-F)/active layer/ N,N'-bis[3-[3-(dimethylamino)propylamino]propyl]perylene-3,4,9,10-tetracarboxylic diimide (PDINN)/silver (Ag) were fabricated to systematically explore the effect of PM6 incorporation on device photovoltaic characteristics. The device performance was carefully optimized through precise control of critical parameters, including the donor-to-acceptor ratio, thermal annealing temperature, along with the spin-coating conditions of the active layer (Tables S3 and S4, Supporting Information). Notably, all devices were fabricated with *o*-XY solvent without any additive. We observed that incorporating PM6 at a ratio as low as 10 wt.% (relative to Y6) led to an obvious enhancement in device performance, which continued to improve with increasing PM6 content and reached a maximum at 30wt.%. Beyond this threshold, further PM6 addition caused rapid performance deterioration. This behavior suggests that while moderate PM6 addition effectively optimizes phase morphology and suppresses excessive crystallization, excessive PM6 disrupts the optimal molecular packing of the host system, confirming its role primarily as a morphological modulator rather than a dominant photoactive component. The current density-voltage (*J*–*V*) characteristics are presented in **Figure** 2a, with the photovoltaic parameters of optimized devices summarized in **Table** 1. The binary devices (BTR-Cl: Y6 = 1.3:1) achieved a PCE of 15.5%, with V_{OC} of 0.842 V, J_{SC} of 26.72 mA cm^{-2}, and *FF* of 69.1%. With 30wt.% PM6 incorporated into the active layer, the BTR-Cl: PM6:Y6 device exhibited a superior PCE of 18.3%, attributed to simultaneous enhancements in both J_{SC} (28.40 mA cm^{-2}) and *FF* (78.4%). To evaluate thickness tolerance, we fabricated

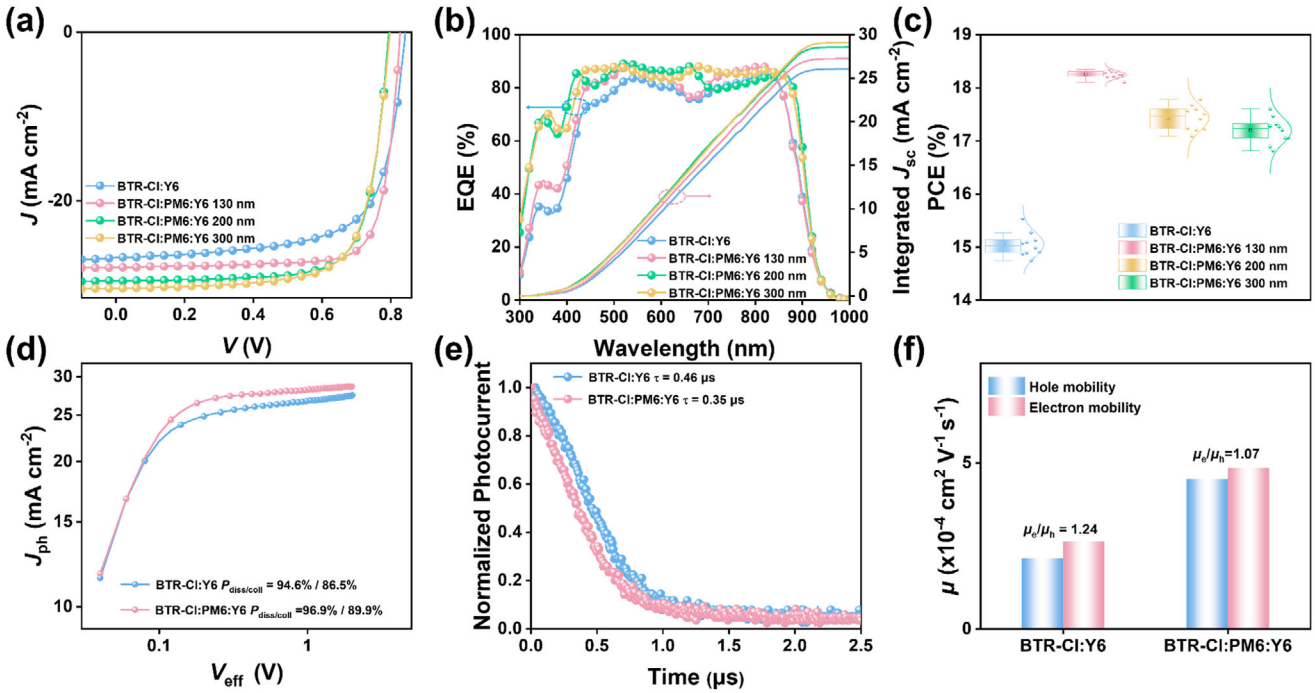

Figure 2. a) The *J–V* characteristics, b) EQE spectra, and c) Statistical particle size distribution diagrams of BTR-Cl: Y6 and BTR-Cl: PM6:Y6 OSCs with different photoactive film thicknesses. d) J_{ph}-V_{eff} curves, e) Transient photocurrent measurements. f) Hole and electron mobilities for BTR-Cl: Y6 and BTR-Cl: PM6:Y6 OSCs.

Table 1. Photovoltaic performance parameters of the devices based on BTR-Cl: Y6 and BTR-Cl: PM6:Y6 with different photoactive film thicknesses, respectively. The average PCEs are obtained from 10 devices.

BHJ	Thickness[nm]	V_{oc} [V]	J_{sc} [mA cm^{-2}]	J_{sc}^{cal} [mA cm^{-2}]	*FF* [%]	$PCE_{max/avg}$ [%]
BTR-Cl:Y6	120	0.842 (0.834 ± 0.009)	26.72 (26.05 ± 0.85)	26.06	69.1 (69.4 ± 2.7)	15.5 (15.1 ± 0.2)
BTR-Cl:PM6:Y6	130	0.822 (0.819 ± 0.004)	28.40 (28.32 ± 0.17)	27.25	78.4 (78.5 ± 0.4)	18.3 (18.2 ± 0.1)
	200	0.800 (0.802 ± 0.006)	29.83 (29.06 ± 0.90)	28.57	74.1 (74.9 ± 1.6)	17.7 (17.4 ± 0.2)
	300	0.798 (0.799 ± 0.003)	30.39 (29.80 ± 0.42)	29.09	72.6 (72.1 ± 0.7)	17.6 (17.2 ± 0.2)

BTR-Cl: PM6:Y6-based devices with active layer thicknesses ranging from 130 to 300 nm (Figure S3, Supporting Information). Although PCE generally decreased with increasing thickness, this system demonstrated remarkable stability – the maximum PCE only declined from 18.3% to 17.6% (Tables S5 and S6, Supporting Information). The J_{SC} values of OSCs are also validated by the EQE spectra (Figure 2b), in which the calculated current densities align well with the trend attained from the *J-V* measurement. Although both of binary and ternary devices had the same photo response region from 300–960 nm, the BTR-Cl: PM6:Y6-based device exhibits slightly higher EQE responses within the 320–840 nm range than the binary device, suggesting a more efficient photoelectric conversion process in the ternary optimal device.[32] Furthermore, the EQE response exhibited both enhancement and red-shift with increasing active layer thickness in ternary devices, consistent with the observed J_{SC} improvement.[9] Figure 2c shows the statistical analysis of PCE distributions across 10 independent devices, confirming the excellent reproducibility for both binary and ternary systems.

Based on the optimized BTR-Cl: PM6:Y6 ternary blends, we successfully fabricated a series-connected module comprising six sub-cells with an effective area of 13.5 cm^2. The device adopts the structure of glass/ITO/3-BPIC-F/BTR-Cl: PM6:Y6/PDINN/Ag (Figure S4, Supporting Information). As shown in Figure S5 (Supporting Information), the champion mini-module demonstrated outstanding performance metrics with a PCE of 12.2%, suggesting the promising potential of such ternary blends for application in large-area devices. To further verify the universality of this morphology modulation strategy, we replaced PM6 with a structurally different polymer PM1 (chemical structure shown in

Figure S6, Supporting Information), and investigated its influence on device performance in the BTR-Cl: Y6-based OSCs.[33] As shown in Table S7 and Figure S7 (Supporting Information), varying the blending ratio of PM1 systematically modulated the photovoltaic properties. With increasing PM1 content, the PCE improved gradually, reaching a peak of 18.0% at the optimal BTR-Cl: PM1:Y6 ratio of 0.9:0.4:1. This improvement was primarily attributed to a higher J_{SC} of 27.48 mA^{-2} and *FF* of 78.3%, both of which are comparable to the best-performing PM6–based devices. The corresponding EQE spectra confirmed enhanced photo-response across 300–900 nm, aligning well with the *J*–*V* measurements. These results indicate that PM1, like PM6, effectively modulates phase morphology and facilitates charge generation and transport. Despite structural differences, both polymers yield similar performance improvements, suggesting that the key lies in disrupting excessive crystallinity and optimizing donor-acceptor interfaces rather than relying on specific chemical interactions.[34,35] This strategy offers a versatile pathway for designing polymeric morphology regulators tailored to various small-molecule systems, enabling the development of efficient and scalable small donor-small acceptor dominated OSCs.

To explore the difference in opto-electrical properties between BTR-Cl: Y6 and BTR-Cl: PM6:Y6 devices, a comprehensive analysis of carrier dynamics was conducted, including exciton dissociation, charge carrier transport, and recombination mechanisms. The dependence of J_{SC} and V_{OC} under varied illumination intensity was analyzed to investigate the bimolecular recombination behavior in optimized devices (Figure S8, Supporting Information). The charge recombination dynamics of these OSCs were evaluated by employing the equation $J_{SC} \propto P_{light}^{\alpha}$, where α indicates the degree of bimolecular recombination within the device. The α values for the binary and ternary devices were determined to be 0.991 and 0.992, respectively. The slightly higher α value for the BTR-Cl: PM6:Y6 device suggests a lower degree of bimolecular recombination compared to the binary counterpart.[36,37] The relationship between V_{OC} and P_{light} can be used to distinguish whether bimolecular recombination (slope of $kT\ q^{-1}$, where k is Boltzmann's constant and T represents the absolute temperature) or trap-assisted recombination (2 $kT\ q^{-1}$) dominates the recombination mechanism.[38,39] The BTR-Cl:PM6:Y6 devices show a small slope of 1.02 $kT\ q^{-1}$, where the BTR-Cl:Y6 blends show a large slope of 1.04 $kT\ q^{-1}$, suggesting weak trap-assisted recombination of BTR-Cl:PM6:Y6 devices.

Besides, the exciton dissociation and charge collection efficiency of OSCs were analyzed by plotting photocurrent (J_{ph}) against the effective applied voltage (V_{eff}) to understand the difference of the J_{SC} of these devices (Figure 2d). The exciton dissociation (P_{diss}) and charge collection efficiencies (P_{coll}) of the BTR-Cl: PM6:Y6 device were estimated to be 96.9%/89.9%, which is slightly higher than the BTR-C: Y6 device (94.6%/86.5%). This result indicates that more efficient photogenerated exciton and charge collection occurred in the ternary device, consistent with its higher J_{SC}.[40] To further quantitatively analyze the charge recombination and extraction behaviors, transient photocurrent (TPC) and transient photovoltage (TPV) were applied to characterize the blend films of BTR-Cl: Y6 and BTR-Cl: PM6:Y6. TPC is employed to assess the photocurrent decay under the short-circuit condition, which reflects the capability of the charge extraction. As shown in Figure 2e, the device of BTR-Cl: PM6:Y6 shows a faster extraction time of 0.35 µs, shorter than that of the BTR-Cl: Y6 device (0.46 µs), manifesting the more efficient charge extraction. The carrier lifetimes (τ) are recorded by TPV decay dynamics under the open-circuit voltage condition, which can further elucidate the recombination of photocarriers. The τ values of BTR-Cl: Y6 and BTR-Cl: PM6:Y6 devices are 92 and 112 µs (Figure S9, Supporting Information), respectively, and the longer τ of the ternary blend illustrates its suppressed charge recombination.[41] The relatively shorter extraction time and longer carrier lifetime of the BTR-Cl: PM6:Y6 devices can well explain its improved J_{SC} and *FF* as compared with the binary one. Moreover, the space-charge-limited current (SCLC) method was used to assess the carrier mobility variation of the blend films (Figure S10, Supporting Information).[42] The μ_h and μ_e of ternary-based devices are 4.51×10^{-4} and 4.85×10^{-4} $cm^2\ V^{-1}\ s^{-1}$, which were higher than those of binary-based devices (2.12×10^{-4} and 2.63×10^{-4} $cm^2\ V^{-1}\ s^{-1}$), as well as more balanced charge transport ($\mu_e/\mu_h = 1.07$) (Figure 2f and Table S8, Supporting Information). The more balanced charge transport and separation supported excellent photovoltaic performance with superior J_{SC} and *FF* values of the BTR-Cl: PM6:Y6-based device. In addition, the detailed energy loss (E_{loss}) analysis (Figures S11 and S12 and Table S9, Supporting Information) shows that introducing PM6 slightly increases the total E_{loss} from 0.552 to 0.572 eV, mainly due to an increase in non-radiative loss (ΔE_3). This moderate rise in E_{loss} accounts for the small V_{OC} decrease, while the concurrently enhanced J_{sc} and *FF* still lead to an overall efficiency improvement.

Device stability is quite an important indicator that can be used to evaluate the performance of OSCs. The thermal stability of the devices was evaluated under continuous heating at 60 °C. As shown in Figure S13 (Supporting Information), the optimized BTR-Cl: PM6:Y6 devices exhibited superior stability compared to the BTR-Cl: Y6 devices. Specifically, the BTR-Cl: PM6:Y6 device retained 80% of its initial PCE after 900 h, whereas the binary BTR-Cl: Y6 device decayed to the same level within 700 h. Furthermore, to evaluate the operational stability of the devices, we conducted photo-stability measurements under continuous one-sun illumination, with measured under light-aging under max power point (MPP) tracking in a nitrogen-filled glovebox. As shown in Figure S14 (Supporting Information), the binary BTR-Cl: Y6 device exhibits a rapid initial degradation, retaining only 80% of its initial PCE after ≈50 h and further declining to 68% after 180 h. In contrast, the ternary BTR-Cl: PM6:Y6 device maintains 80% of its initial PCE even after 180 h. These results indicate that the incorporation of PM6 significantly enhances the intrinsic stability of the devices, further highlighting the practical potential of this strategy.

To elucidate the film formation dynamics and crystallization behavior of active layers, we performed in situ UV–vis absorption spectroscopy during spin-coating for both BTR-Cl: Y6 and BTR-Cl: PM6:Y6 blend films (**Figure 3a–c**). The film formation process exhibits three distinct stages: (I) Solution state with invariant donor/acceptor absorption peaks; (II) Nucleation/growth stage characterized by red-shifting peaks during solvent evaporation and molecular aggregation; and (III) Stable film state after complete solvent removal.[43] Notably, the duration of Stage II differs significantly between the two systems. In the binary BTR-Cl: Y6 blend, the aggregation time for Y6 is ≈1.06 s, while BTR-Cl

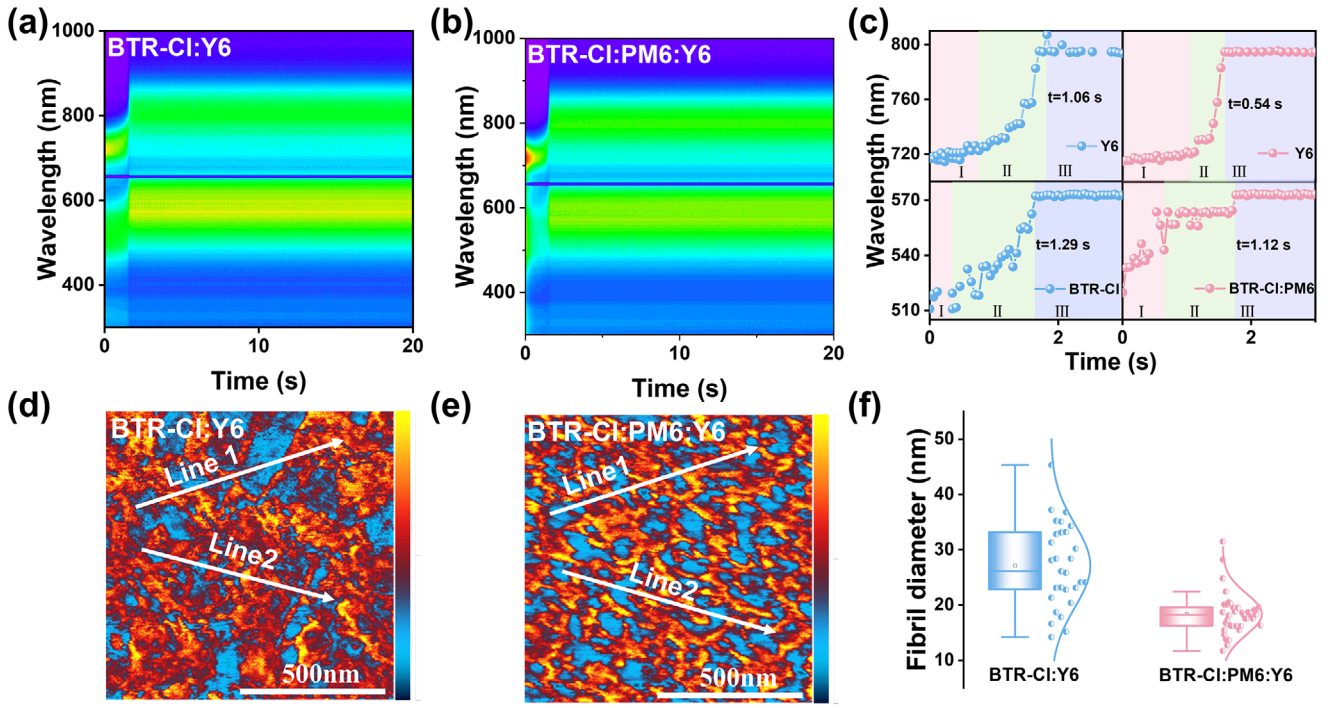

Figure 3. Time-dependent contour maps of in situ UV–vis absorption spectra of a) BTR-Cl: Y6 and b) BTR-Cl: PM6:Y6 films during spin coating. c) Time evolution of the peak location of BTR-Cl; BTR-Cl: PM6 and Y6. AFM-IR images of d) BTR-Cl: Y6 and e) BTR-Cl: PM6:Y6 blend films. f) The statistical distribution of the fibril diameter for BTR-Cl: Y6 and BTR-Cl: PM6:Y6 films.

exhibits a nucleation duration of 1.29 s. In contrast, the BTR-Cl: PM6:Y6 blend shows markedly faster crystallization behavior, with the Y6 peak stabilizing within 0.54 s and the donor transition completing in 1.12 s. This shortened crystallization time suggests that the incorporation of PM6 facilitates faster molecular ordering and mitigates excessive molecular aggregation typically caused by slow drying kinetics associated with non-halogenated solvents.[29] In the ternary blend, the donor absorption peak exhibits a two-step red-shift behavior during Stage II. The initial rapid red-shift likely corresponds to local nucleation and short-range aggregation, promoted by the interaction between PM6 and BTR-Cl. This is followed by a brief plateau, where the red-shift temporarily slows down, possibly due to spatial constraints or kinetic stabilization. Subsequently, a second red-shift occurs, which can be attributed to further molecular rearrangement and the development of long-range order.[44] This two-step evolution reveals that PM6 induces a multi-stage packing process, which not only accelerates crystallization but also enables a more refined and ordered morphology.[18,29,35] These kinetic advantages synergistically enhance exciton dissociation and charge transport, directly correlating with the superior photovoltaic performance of ternary OSCs. Complementary in situ thermal annealing UV–vis measurements (Figure S15, Supporting Information) reveal the donor absorption decay time shortens from 2 to 1 s in ternary blends, further evidencing PM6's role in accelerating molecular aggregation throughout the entire film evolution process.

Furthermore, atomic force microscopy (AFM) was employed to investigate the effect of PM6 on the surface morphology of the blends. As demonstrated in Figures S16 and S17 (Supporting Information), the ternary blend exhibited a significantly lower root-mean-square roughness (R_q) value (1.25 nm) compared to the binary blend (1.71 nm). This reduction in surface roughness suggests that PM6 promotes finer mixing and suppresses the formation of large-scale aggregates within the blend.[45] This result is consistent with the accelerated and more controlled crystallization dynamics revealed by the in situ spin-coating UV–vis measurements. To further elucidate the nanoscale phase structure of the active layers, AFM-IR was performed using the characteristic absorption at 1059 cm^{-1} to selectively probe the donor BTR-Cl (Figure S18, Supporting Information). As shown in Figure 3d,e, the red regions represent the distribution of BTR-Cl, while the blue regions correspond to Y6 or Y6/PM6 in the two respective blend films. Strikingly distinct morphologies were observed between the two blends. The binary blend displayed a morphology dominated by large and irregular crystalline domains, consistent with the high crystallinity and strong aggregation tendency of both small-molecule components. In contrast, the BTR-Cl: PM6:Y6 film exhibited a more continuous and interconnected morphology with reduced domain size. This morphological transition can be attributed to the incorporation of PM6, whose flexible polymer backbone effectively suppresses the over-crystallization of BTR-Cl and facilitates better miscibility with Y6. As quantified in Figure 3f and Figure S19 (Supporting Information), the fibril diameter in the ternary blend (18.4 ± 3.7 nm) is slightly smaller and more uniform than that in the binary blend (20.1 ± 7.5 nm), indicating improved phase refinement and suppressed macro-phase separation.[46,47] Contact-angle analysis indicates that PM6 exhibits an intermediate surface energy between BTR-Cl and Y6, enabling it to act as an

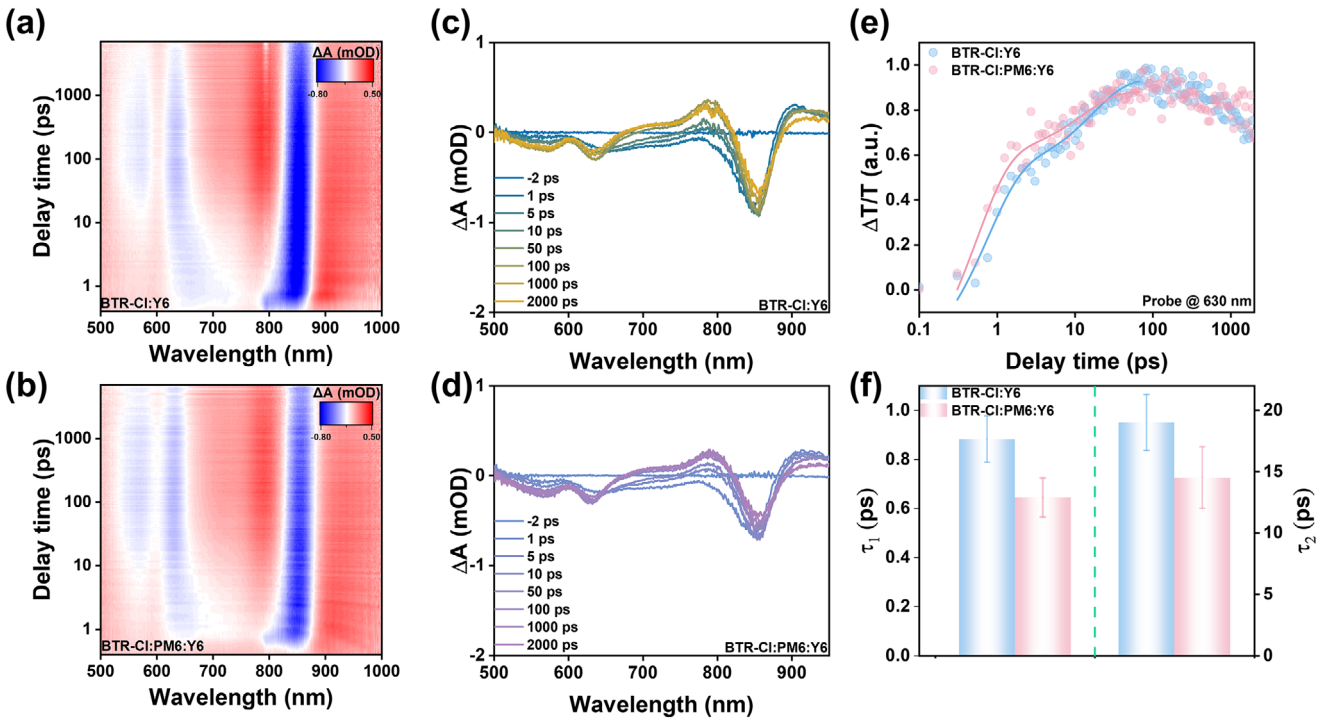

Figure 4. 2D color plots of TA spectra of a) BTR-Cl: Y6 and b) BTR-Cl: PM6:Y6 blend film upon excitation at 800 nm. Transient absorption spectra at different probe delay times of c) BTR-Cl: Y6 and d) BTR-Cl: PM6:Y6 blend film. e) Kinetic traces for the GSB of the donor in the binary and ternary blend films probed at 630 nm, and f) the values of τ_1 and τ_2 in the blend films.

interfacial compatibilizer. This reduces donor–acceptor interfacial tension, improves miscibility, and correlates well with the refined morphology and improved photovoltaic performance observed in the ternary devices (Figure S20 and Table S10, Supporting Information). These findings, in conjunction with the AFM height mapping and in situ UV–Vis results, suggest that PM6 plays a critical role in regulating the crystallization kinetics and promoting a finely mixed morphology favorable for efficient exciton dissociation and charge transport.

To gain molecular-level insights into the aggregation behavior of the active layer components, molecular dynamics (MD) simulations were performed for both the BTR-Cl: Y6 and BTR-Cl: PM6:Y6 blends.[17,34,47] As shown in Figure S21 (Supporting Information), the binary blend exhibits large, well-defined crystalline domains, indicating strong intermolecular interactions and pronounced aggregation between the small-molecule donor BTR-Cl and acceptor Y6. In contrast, the BTR-Cl domains in the BTR-Cl: PM6:Y6 blend film are significantly reduced, while forming more D/A interfaces with Y6. This observation is consistent with the experimental findings; the incorporation of PM6 disrupts the extended crystallization of BTR-Cl and moderates the strong phase separation between donor and acceptor domains.[29,35] The polymer chains of PM6 act as a capitalizing agent, disturbing excessive ordering while promoting more homogeneous mixing and better donor–acceptor interface contact. These molecular simulation results align well with the experimental observations and further confirm that PM6 plays a crucial role in modulating molecular packing, reducing domain size, and achieving a more refined morphology beneficial for charge transport and device performance.

We employed ultrafast transient absorption (TA) spectroscopy to gain deeper physical insights into the exciton dynamics and charge transfer processes. The 2D color plots depicting the TA images for the blend films are presented in **Figure** 4a,b, while the corresponding kinetic curves at 630 and 850 nm are displayed in Figure 4c,d. An excitation wavelength of 800 nm was used to selectively excite Y6 molecules in the blend films, both with and without PM6 addition. From the TA profiles at various delay times, it is evident that as the acceptor ground-state bleach (GSB) signal at ≈ 850 nm decays, the bleaching peak (850 nm) of the acceptor decreases with time, while the GSB peak of the donor increases, indicating an effective hole-transfer process from the acceptor to the donor. The exponential fitting of the GSB kinetics at 630 nm, shown in Figure 4e,f, demonstrates the hole transfer dynamics. The fast component (τ_1) was attributed to exciton dissociation dynamics at the mixing domain or interface, while the slow component (τ_2) represented diffusion-mediated processes within the crystalline domain.[5,48] The hole transfer process in the binary and ternary blend films showed τ_1 values of 0.88 and 0.64 ps, and τ_2 values of 19.01 and 14.50 ps, respectively (Table S11, Supporting Information). The relatively smaller τ_1 and τ_2 values for the BTR-Cl: PM6:Y6 blend indicate that exciton dissociation and diffusion are efficient, which is conducive to suppressing recombination and thus enhancing J_{SC} and *FF*. According to Marcus theory, the rate of charge transfer depends on the electronic coupling (H_{DA}) between donor and acceptor molecules, which is highly sensitive to their intermolecular distance.[49,50] Therefore, the significantly reduced τ_1 in the BTR-Cl: PM6:Y6 blend can be attributed to a more condensed intermixed morphology that facilitates faster exciton dissociation at the donor–acceptor interface,

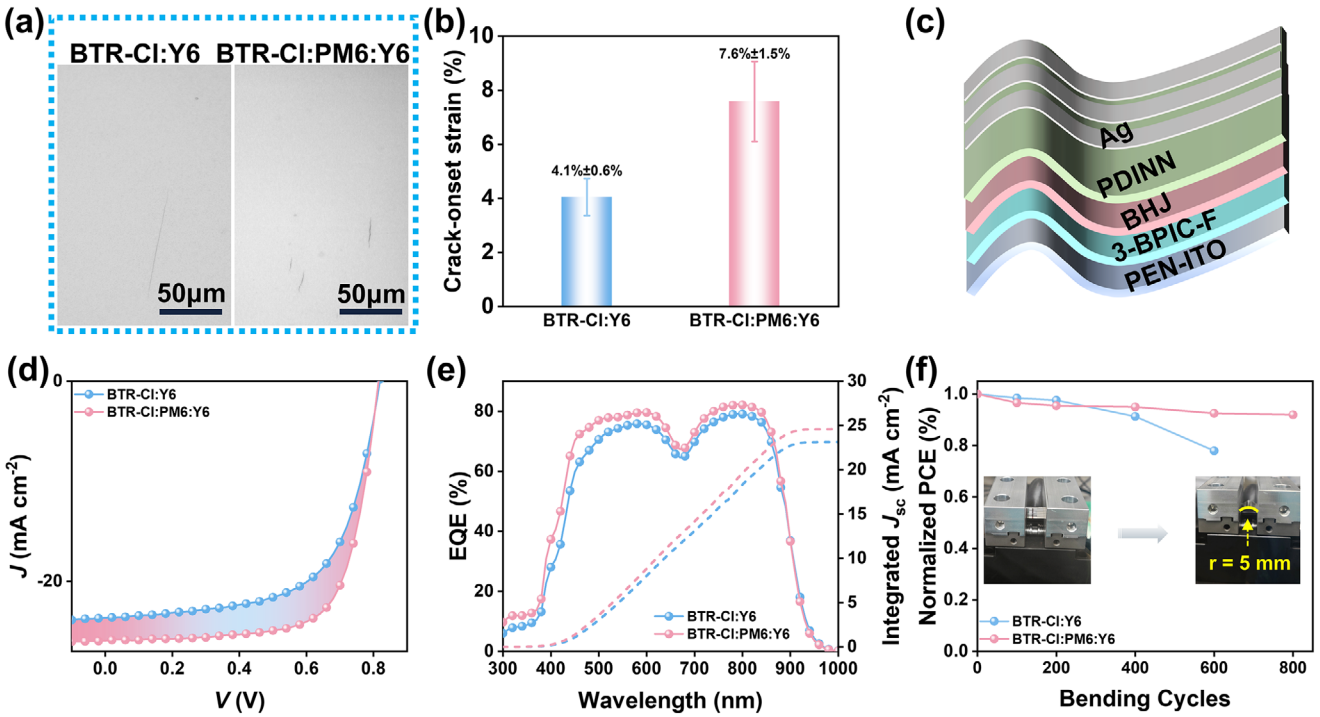

Figure 5. a) Optical micrographs of the formed cracks of BTR-Cl: Y6 and BTR-Cl: PM6:Y6 blend films by stretching on PDMS substrates at their respective crack-onset strains. b) Histograms of COS of two blend films. c) Device structure of flexible devices. d) The *J–V* characteristics, e) EQE spectra of BTR-Cl: Y6 and BTR-Cl: PM6:Y6-based flexible devices. f) Normalized PCE value for the flexible devices as a function of bending cycles with a radius of 5 mm.

Table 2. Photovoltaic performance parameters of the flexible devices based on BTR-Cl: Y6 and BTR-Cl: PM6:Y6, respectively. The average PCEs are obtained from 10 devices.

BHJ	V_{oc} [V]	J_{sc} [mA cm^{-2}]	J_{sc}^{cal} [mA cm^{-2}]	*FF* [%]	$PCE_{max/avg}$ [%]
BTR-Cl:Y6	0.819 (0.823 ± 0.006)	23.67 (23.75 ± 0.23)	23.14	63.2 (59.8 ± 1.7)	12.3 (11.7 ± 0.3)
BTR-Cl:PM6:Y6	0.815 (0.811 ± 0.002)	25.92 (25.99 ± 0.12)	24.60	70.7 (69.4 ± 0.8)	14.9 (14.6 ± 0.2)

as demonstrated in the preceding morphology analysis. Meanwhile, the shortened τ_2 indicates more efficient charge transport within the ordered domains, likely due to reduced phase separation. These results collectively demonstrate that the incorporation of PM6 promotes more favorable morphology and charge dynamics, leading to more efficient charge generation and contributing to the observed improvements in J_{SC} and *FF*.

Flexible OSCs based on all-small-molecule systems typically suffer from poor mechanical robustness due to the intrinsic brittleness and excessive crystallinity of small-molecule semiconductors.[6,20,26] In this work, a small amount of polymer PM6 was added to the BTR-Cl: Y6 system, where it could simultaneously act as a morphological and mechanical modulator. To quantitatively assess the mechanical enhancement, we evaluated the COS of blend films using the film-on-elastomer (FOE) method.[51,52] As shown in **Figure** 5a,b, the BTR-Cl:Y6 film exhibited a low COS of (4.1 ± 0.6)%, while the BTR-Cl:PM6:Y6 film showed a significantly increased COS of (7.6 ± 1.5)%, confirming improved ductility of the active layer upon PM6 incorporation. The enhanced mechanical flexibility is attributed to the disruption of excessive crystalline domains and the formation of a more resilient polymer network within the blend. With those in mind, we fabricated flexible OSCs by replacing rigid glass/ITO with flexible polyethylene naphthalate (PEN)/ITO substrates, while keeping other layers and fabrication conditions unchanged (Figure 5c). As shown in Figure 5d and **Table** 2, the binary flexible device achieved a PCE of 12.3% (J_{SC} = 23.67 mA cm^{-2}, *FF* = 63.2%). Upon introducing PM6, the ternary device exhibited an enhanced PCE of 14.9%, with a higher J_{SC} of 25.92 mA cm^{-2} and *FF* of 70.7%, closely matching the performance observed in rigid counterparts. Detailed photovoltaic parameters of optimal BTR-Cl: Y6 and BTR-Cl: PM6:Y6-based flexible devices are summarized in Table S12 (Supporting Information). The corresponding EQE spectra (Figure 5e) also showed improved response in the 400–850 nm range for the ternary devices, consistent with the trend of its enhanced photocurrent. Finally, bending durability tests (r = 5 mm) were carried out to evaluate long-term mechanical reliability. As illustrated in Figure 5f, the ternary

flexible device retained ≈92% of its initial efficiency after 800 bending cycles, while the binary counterpart dropped to ≈78% after 600 cycles. These results clearly demonstrate that polymer incorporation not only improves mechanical resilience but also enables flexible OSCs with high efficiency and excellent stability, offering a practical solution for the mechanical limitations of all-small-molecule systems in flexible electronics.

3. Conclusion

In summary, the introducing of a small amount of polymer PM6 into small donor-small acceptor dominated OSCs, successfully addresses a long-standing critical challenge in this field. It effectively regulates the difficulty in achieving ideal phase separation between small-molecular donor and acceptor, which is often hindered by their high miscibility. This regulation optimizes the active layer morphology and significantly enhances exciton dissociation and charge transport efficiency by promoting face-on orientation and the formation of continuous fiber networks, resulting in a high efficiency of 18.3% for the BTR-Cl: PM6:Y6–based device. This efficiency ranks among the highest reported for small donor-small acceptor dominated OSCs processed from non-halogenated solvents. The BTR-Cl: PM6:Y6 system also demonstrates excellent thickness insensitivity and potential for large-area fabrication (a 13.5 cm^2 mini-module with an efficiency of 12.2%). Enabled by PM6's long-chain structure, the flexible ternary device achieved a high PCE of 14.9% while maintaining 92% initial efficiency over 800 bending cycles. Furthermore, the incorporation of polymer PM1 into the BTR-Cl: Y6 system achieved a PCE of 18.0%, further validating the effectiveness of this strategy. Although PM6/PM1-polymer demonstrates advantages in enhancing multiple aspects of small donor-small acceptor dominated active layer devices, its batch-to-batch variation remains a significant challenge. Oligomers combine the structural precision and batch reproducibility of small molecules with the superior film-forming capability and morphological stability of polymers, making them ideal candidates for morphology control in small donor-small acceptor dominated OSCs. Therefore, designing oligomeric materials that combine the morphology-regulating advantages of polymers with the high purity and facile crystallizable of small molecules will be a crucial direction for further enhancing the overall performance of small donor-small acceptor dominated OSCs and realizing more efficient and stable devices.

Supporting Information

Supporting Information is available from the Wiley Online Library or from the author.

Acknowledgements

J.W. and W.Z. contributed equally to this work. The authors gratefully acknowledge the financial support from the Ministry of Science and Technology of the People's Republic of China (2023YFE0210400), National Natural Science Foundation of China (22361132530, 52573199, and 52303237), Natural Science Foundation of Tianjin (24JCYBJC01540), and the Fundamental Research Funds for the Central Universities of Nankai University (023-63253172). B. Kan would like to acknowledge Prof. Alex Jen for his outstanding contributions to the field. This work is respectfully dedicated in honor of his 70th birthday.

Conflict of Interest

The authors declare no conflict of interest

Data Availability Statement

The data that support the findings of this study are available from the corresponding author upon reasonable request.

Keywords

morphology regulation, non-halogenated solvent, organic solar cells, small-molecular materials, power conversion efficiency

Received: August 15, 2025
Revised: September 6, 2025
Published online: September 18, 2025

[1] X. Yu, S. Yang, Z. Shao, L. Xie, Z. Wang, P. Ding, T. Liu, J. Wu, X. Cao, J. Zhu, F. Chen, G. Chen, D. Yang, Z. Ge, *Sci. China Chem.* **2025**, *68*, https://doi.org/10.1007/s11426-025-2723-9.
[2] C. Li, Y. Cai, P. Hu, T. Liu, L. Zhu, R. Zeng, F. Han, M. Zhang, M. Zhang, J. Lv, Y. Ma, D. Han, M. Zhang, Q. Lin, J. Xu, N. Yu, J. Qiao, J. Wang, X. Zhang, J. Xia, Z. Tang, L. Ye, X. Li, Z. Xu, X. Hao, Q. Peng, F. Liu, L. Guo, H. Huang, *Nat. Mater.* **2025**, https://doi.org/10.1038/s41563-025-02305-8.
[3] X. Wan, C. Li, M. Zhang, Y. Chen, *Chem. Soc. Rev.* **2020**, *49*, 2828.
[4] R. Ma, Z. Luo, Y. Zhang, L. Zhan, T. Jia, P. Cheng, C. Yan, Q. Fan, S. Liu, L. Ye, G. Zhang, X. Xu, W. Gao, Y. Wu, J. Wu, Y. Li, Y. Liu, F. Liu, J. Song, H. Chen, W. Chen, X. Zhang, Y. Liu, J. Yuan, Q. Liu, Z. Kan, H. Yin, X. Li, Y. Ma, D. Deng, et al., *Sci. China Mater.* **2025**, *68*, 1689.
[5] T. Chen, Y. Zhang, W. Zhao, Y. Zhong, W. Feng, B. Lan, X. Dong, J. Yang, J. Zhang, K. Han, G. Long, B. Kan, Y. Chen, *Sci. China Chem.* **2025**, *68*, 3260.
[6] T. Zhang, C. An, P. Bi, K. Xian, Z. Chen, J. Wang, Y. Xu, J. Dai, L. Ma, G. Wang, X. Hao, L. Ye, S. Zhang, J. Hou, *Energy Environ. Sci.* **2024**, *17*, 3927.
[7] R. Ma, X. Jiang, T. A. Dela Peña, W. Gao, J. Wu, M. Li, S. V. Roth, P. Müller-Buschbaum, G. Li, *Adv. Mater.* **2024**, *36*, 2405005.
[8] Y. Gao, X. Yang, R. Sun, L.-Y. Xu, Z. Chen, M. Zhang, H. Zhu, J. Min, *Joule* **2023**, *7*, 2845.
[9] Y. Gao, L.-Y. Xu, X. Chen, B. Xiao, W. Gao, J. Xia, R. Sun, J. Min, *Energy Environ. Sci.* **2025**, *18*, 7302.
[10] X. Yang, Y. Gao, L.-Y. Xu, X. Wu, X. Chen, Y. Shao, B. Xiao, S. Liu, J. Xia, R. Sun, J. Min, *Energy Environ. Sci.* **2024**, *17*, 5962.
[11] L. Liu, H. Li, J. Xie, Z. Yang, Y. Bai, M. Li, Z. Huang, K. Zhang, F. Huang, *Adv. Mater.* **2025**, *37*, 202500352.
[12] B. Du, M. Ma, P. Zhang, S. Wu, H. Bin, Y. Li, *ACS Appl. Mater. Interfaces* **2024**, *16*, 2564.
[13] W. Gao, R. Ma, T. A. Dela Peña, C. Yan, H. Li, M. Li, J. Wu, P. Cheng, C. Zhong, Z. Wei, A. K. Y. Jen, G. Li, *Nat. Commun.* **2024**, *15*, 1946.
[14] Y. Liu, J. Zhang, C. Tian, Y. Shen, T. Wang, H. Zhang, C. He, D. Qiu, Y. Shi, Z. Wei, *Adv. Funct. Mater.* **2023**, *33*, 2300778.
[15] I. Burgués-Ceballos, F. Machui, J. Min, T. Ameri, M. M. Voigt, Y. N. Luponosov, S. A. Ponomarenko, P. D. Lacharmoise, M. Campoy-Quiles, C. J. Brabec, *Adv. Funct. Mater.* **2013**, *24*, 1449.
[16] R. Ma, X. Jiang, J. Fu, T. Zhu, C. Yan, K. Wu, P. Müller-Buschbaum, G. Li, *Energy Environ. Sci.* **2023**, *16*, 2316.
[17] J. Wang, P. Wang, T. Chen, W. Zhao, J. Wang, B. Lan, W. Feng, H. Liu, Y. Liu, X. Wan, G. Long, B. Kan, Y. Chen, *Angew. Chem., Int. Ed.* **2025**, *64*, 202423562.

[18] X. Cheng, Z. Liang, S. Liang, X. Zhang, J. Xu, Y. Xu, W. Ni, M. Li, Y. Geng, *J. Mater. Chem. A* **2023**, *11*, 13984.
[19] R. Ma, B. Zou, Y. Hai, Y. Luo, Z. Luo, J. Wu, H. Yan, G. Li, *Adv. Mater.* **2025**, *37*, 2500861.
[20] Y. Bai, S. Li, Q. Wang, Q. Chen, Z. Zhang, S. Meng, Y. Zang, H. Fu, L. Xue, L. Ye, Z.-G. Zhang, *Nati. Sci. Rev.* **2025**, *12*, nwaf019.
[21] S. Xu, Q. He, X. Xue, J. Deng, F. Han, F. Xie, X. Jiao, L. Zhou, R. Zeng, Z. Wang, M. Zhang, L. Zhu, H. Jing, Y. Zhang, F. Liu, *Angew. Chem., Int. Ed.* **2025**, *64*, 202507616.
[22] W. Liu, Y. Nai, J. Yuan, C. Zhang, W. Chen, R. Sun, Q. Xue, H. Zhu, Y. Zhong, K. Gu, J. Yang, J. Min, S. Xiao, J. He, J. Zhang, K. Han, X. Guo, Y. Zou, *Macromolecules* **2025**, *58*, 6315.
[23] Z. Zhang, Q. Chen, C. Zhang, W. L. Tan, G. Zhang, Z. Bu, C. Xiao, X. Shen, Z. Tang, C. R. McNeill, W. Li, *Adv. Funct. Mater.* **2024**, *34*, 2401823.
[24] Y. Liu, X. Wan, F. Wang, J. Zhou, G. Long, J. Tian, Y. Chen, *Adv. Mater.* **2011**, *23*, 5387.
[25] J. Liu, X. Liao, W. Zhou, F. Ding, J. Deng, S. Y. Jeong, H. Y. Woo, J. Wei, L. Chen, *Sci. China Chem.* **2025**, *68*, 3647.
[26] Q. Ye, W. Song, Y. Bai, Z. Chen, P. Ding, J. Ge, Y. Meng, B. Han, X. Zhou, *Z. Ge, Energy Environ. Sci.* **2025**, *18*, 4373.
[27] X. Liao, Q. Xie, Y. Guo, Q. He, Z. Chen, N. Yu, P. Zhu, Y. Cui, Z. Ma, X. Xu, H. Zhu, Y. Chen, *Energy Environ. Sci.* **2022**, *15*, 384.
[28] H. Tian, K. Sun, D. Luo, Y. Wang, Z. Chen, L. Yu, G. Zhang, C. Yang, Z. Luo, *Sci. China Chem.* **2025**, *68*, https://doi.org/10.1007/s11426-025-2671-6.
[29] E. Feng, C. Zhang, J. Chang, F. Zhao, B. Hu, Y. Han, M. Sha, H. Li, X.-J. Du, C. Long, Y. Ding, Z.-J. Yang, H. Yin, Q. Luo, C.-Q. Ma, G. Lu, Z. Ma, X.-T. Hao, J. Yang, *ACS Nano* **2024**, *18*, 28026.
[30] X. Wang, N. Wei, Y. Chen, G. Ran, A. Zhang, H. Lu, Z. Wei, Y. Liu, W. Zhang, *Z. Bo, Nati. Sci. Rev.* **2024**, *11*, nwae258.
[31] B. Lan, S. Yuan, Y. Zhong, W. Zhao, J. Wang, W. Shi, G. Long, O. A. Rakitin, J. Zhang, K. Han, B. Kan, Y. Chen, *Mater. Horiz* **2025**, *12*, 3349.
[32] J. Qin, Z. Chen, P. Bi, Y. Yang, J. Zhang, Z. Huang, Z. Wei, C. An, H. Yao, X. Hao, T. Zhang, Y. Cui, L. Hong, C. Liu, Y. Zu, C. He, J. Hou, *Energy Environ. Sci.* **2021**, *14*, 5903.
[33] H. Tian, Y. Ni, W. Zhang, Y. Xu, B. Zheng, S. Y. Jeong, S. Wu, Z. Ma, X. Du, X. Hao, H. Y. Woo, L. Huo, X. Ma, F. Zhang, *Energy Environ. Sci.* **2024**, *17*, 5173.
[34] W. Feng, T. Chen, Y. Li, T. Duan, X. Jiang, C. Zhong, Y. Zhang, J. Yu, G. Lu, X. Wan, B. Kan, Y. Chen, *Angew. Chem., Int. Ed.* **2024**, *63*, 202316698.
[35] Z. Zhang, D. Deng, Y. Li, J. Ding, Q. Wu, L. Zhang, G. Zhang, M. J. Iqbal, R. Wang, J. Zhang, X. Qiu, Z. Wei, *Adv. Energy Mater.* **2021**, *12*, 2102394.
[36] S. Yuan, B. Lan, X. Ji, J. Wang, W. Zhao, G. Long, X. Wan, B. Kan, Y. Chen, *J. Mater. Chem. C* **2025**, *13*, 938.
[37] W. Zhou, J. Wang, W. Shi, J. Wang, S. Yuan, B. Lan, B. Kan, *J. Mater. Chem. C* **2025**, *13*, 13768.
[38] S. R. Cowan, A. Roy, A. J. Heeger, *Phys. Rev. B* **2010**, *82*, 245207.
[39] C. M. Proctor, M. Kuik, T.-Q. Nguyen, *Prog. Polym. Sci.* **2013**, *38*, 1941.
[40] W. Shi, Q. Han, Y. Zhu, Y. Xia, T. He, S. Wang, L. Li, W. Ma, G. Long, G. Li, Z. Yao, C. Li, X. Wan, Y. Chen, *Nati. Sci. Rev.* **2025**, *12*, nwae409.
[41] Y. Bai, T. Chen, X. Ji, J. Wang, W. Zhao, S. Yuan, Y. Zhang, G. Long, Z. Zhang, X. Wan, B. Kan, Y. Chen, *Adv. Energy Mater.* **2024**, *14*, 2400938.
[42] J. Sun, R. Ma, X. Yang, X. Xie, D. Jiang, Y. Meng, Y. Li, F. Cui, M. Xiao, K. Zhang, Y. Chen, X. Xia, M. Zhang, X. Du, L. Ye, H. Ma, K. Gao, F. Chen, G. Li, X. Hao, H. Yin, *Nati. Sci. Rev.* **2025**, *12*, nwae385.
[43] R. Gong, Q. Yan, Z. Xing, H. Wang, L. Tan, X. Meng, X. Hu, Y. Chen, *Adv. Mater.* **2025**, *37*, 2501033.
[44] Z. Fu, J. W. Qiao, F. Z. Cui, W. Q. Zhang, L. H. Wang, P. Lu, H. Yin, X. Y. Du, W. Qin, X. T. Hao, *Adv. Mater.* **2024**, *36*, 2313532.
[45] P. Ding, X. Rong, D. Yang, X. Yu, Z. Shao, H. Wang, X. Liao, X. Cao, J. Wu, L. Xie, J. Zhu, F. Chen, G. Chen, Y. Huang, Z. Ge, *Energy Environ. Sci.* **2025**, *18*, 6548.
[46] L. Zhu, M. Zhang, J. Xu, C. Li, J. Yan, G. Zhou, W. Zhong, T. Hao, J. Song, X. Xue, Z. Zhou, R. Zeng, H. Zhu, C.-C. Chen, R. C. I. MacKenzie, Y. Zou, J. Nelson, Y. Zhang, Y. Sun, F. Liu, *Nat. Mater.* **2022**, *21*, 656.
[47] X. Cao, Z. Xu, R. Wang, J. Guo, W. Zhao, Y. Zhang, Z. Yao, Y. Guo, G. Long, X. Wan, Y. Chen, *Adv. Mater.* **2025**, *37*, 2503131.
[48] M. Zhang, L. Zhu, G. Zhou, T. Hao, C. Qiu, Z. Zhao, Q. Hu, B. W. Larson, H. Zhu, Z. Ma, Z. Tang, W. Feng, Y. Zhang, T. P. Russell, F. Liu, *Nat. Commun. 2021 12*, 309.
[49] R. A. Marcus, *J. Phys. Chem.* **1956**, *24*, 966.
[50] H. Oberhofer, J. Blumberger, *J. Phys. Chem.* **2010**, *133*, 244105.
[51] K. Xian, K. Zhang, T. Zhang, K. Zhou, Z. Zhang, J. Hou, H. Zhang, Y. Geng, L. Ye, *Energy Environ. Sci.* **2025**, *18*, 2570.
[52] L. Pei, D. Han, Y. Wang, M. Gao, J. Wu, C. Sun, M. Yu, Y. X. Wang, H. Ke, X. Li, L. Ye, *Adv. Funct. Mater.* **2025**, 2425892.